Texas A&M University
Mechanical Engineering Department
Turbomachinery Laboratory
Tribology Group

GAS LABYRINTH SEALS: IMPROVED PREDICTION OF LEAKAGE IN GAS LABYRINTH SEALS USING AN UPDATED KINETIC ENERGY CARRY-OVER COEFFICIENT

TRC-SEAL-01-19

Research Progress Report to the Turbomachinery Research Consortium
by

Luis San Andrés
Mast-Childs Chair Professor
Principal Investigator

Tingcheng Wu
Research Assistant

May 2019

PRESSING NEEDS FOR SEALS /BEARING SOFTWARE DEVELOPMENT/UPDATE

TRC Project, TEES # 28-258124-00027

EXECUTIVE SUMMARY

Bulk-flow predictive models, though simple and fast, fail to accurately predict the performance of gas labyrinth seals (LSs). Presently, a CFD analysis quantifies the effects of labyrinth seal (LS) tip clearance (C_r) and operating conditions on the kinetic energy carry-over coefficient (μ_{1i}) as per mass flow prediction. The analysis aims to improve the prediction of LS mass flow rate. A fourteen teeth on stator LS seal (L/D=0.29) with clearance C_r=1/733 D is selected for analysis. The seal operates at nominal supply and discharge pressures equal to 73 bar and 51 bar, respectively, and at a rotor speed of 12 krpm (surface speed=138 m/s.).

The analysis models the seal with a fine mesh of a few million nodes and a commercial CFD code calculates the flow field for the nominal operating conditions, as well as for changes in clearance, 80% to 200% of the nominal C_r, a gas supply pressure ranging from 60 bar to 100 bar, and along with various discharge pressures producing a pressure ratio (PR) ranging from 0.40 to 0.85. The numerous predictions output the mass flow rate as well as the bulk-flow velocity and cavity pressures distribution. The kinetic energy carry-over coefficient (μ_{1i}) increases with respect to the seal radial clearance (C_r); whereas μ_{1i} shows parabolic correlation with the pressure ratio PR. At a relatively lower PR, μ_{1i} first increases with an increase in PR, and further increase in the PR leads to a decrease in μ_{1i}. μ_{1i} is only sensitive to the pressure ratio, and not to the magnitude of either the supply pressure or the discharge pressure.

Lastly, for use with the classical Neumann's leakage model, an analysis of the CFD predictions produces a new coeffient μ_{1i}, a function of the seal geometry and the inlet/exit pressure ratio condition. Later, integration of the found μ_{1i} correlation into a BFM code improves its accuracy to predict LS mass flow rate. A TOS LS tested by Ertas et al. (2012) serves to further validate successfully the modified leakage model. XLLaby®, part of the XLTRC2 suite, is modified to include the derived new coefficient μ_{1i}, and which utimately assists to deliver more accurate flow predictions.

TABLE OF CONTENTS

LIST OF FIGURES

LIST OF TABLES

1. INTRODUCTION[1]

Commonly found in gas and steam turbines and compressors, labyrinth seals (LS) control the leakage (secondary flow) from a high pressure region to a low pressure region. A typical LS comprises of cavities and teeth facing a spinning rotor. The tortuous gas flow path through the cavities induces a pressure drop and restricts leakage. A see-through LS has all the teeth either on the rotor (TOR) or on the stator (TOS), while an interlocking design (ILS) has teeth on the rotor as well as on the stator. LS leakage depends on seal geometry (tooth shape, pitch/depth, and number of cavities), gas type, and operating shaft speed, pressure and temperature (inlet and outlet).

During operation, seals do not just restrict a secondary flow but also produce reaction forces acting on the rotor. These forces may introduce an instability into a rotating system, as reported in Refs. [1, 2] for example. Therefore, the ability to accurately predict LS leakage and rotordynamic force coefficients is crucial for the efficient and rotordynamic stable operation of turbomachinery.

Forces developed by LSs are typically lower than those from liquid seals. For small amplitude rotor displacements (X,Y) about its centered condition, the force components (F_X, F_Y) are modeled as

$$-\begin{bmatrix} F_X \\ F_Y \end{bmatrix} = \begin{bmatrix} K_{(\omega)} & k_{(\omega)} \\ -k_{(\omega)} & K_{(\omega)} \end{bmatrix} \begin{bmatrix} X \\ Y \end{bmatrix} + \begin{bmatrix} C_{(\omega)} & c_{(\omega)} \\ -c_{(\omega)} & C_{(\omega)} \end{bmatrix} \begin{bmatrix} \dot{X} \\ \dot{Y} \end{bmatrix} \tag{1}$$

Where, $K_{(\omega)}$ and $C_{(\omega)}$ stand for the direct stiffness and damping coefficients; $k_{(\omega)}$ and $c_{(\omega)}$ for the cross-coupled stiffness and damping, respectively. In a gas seal these force coefficients are functions of the excitation frequency (ω). LSs, because of the working gas small density[2], offer negligible added mass terms.

The literature is profuse on detailing experimental results and models for LS leakage and rotordynamic coefficients [2]. Most research focuses on "see-through" LSs; that is seals with a uniform clearance and all the teeth on either the stator (TOS), see Figure 1(a), or all teeth on the rotor (TOR), see Figure 1(b).

[1] Reproduced from Ph.D. proposal of Tingcheng Wu (2018).

[2] This assertion is not valid for seals handing sCO_2 (at high pressures), for example.

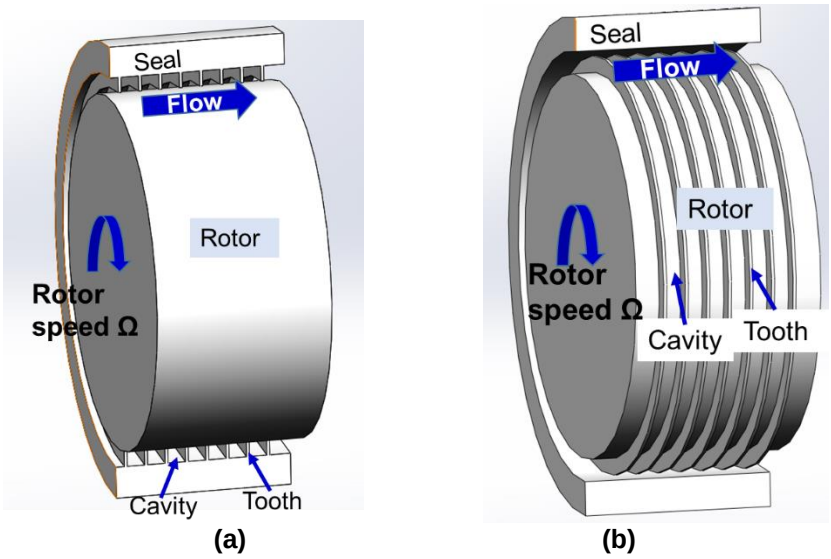

Figure 1. See through labyrinth gas seal: (a) teeth on stator (TOS), (b) teeth on rotor (TOR).

The interlocking labyrinth seal (ILS) configuration, as shown in Figure 2, increases the overall flow resistance as the gas passes through a narrow clearance. Therefore, the ILS relatively leaks less compared to conventional TOS and TOR LS designs. As shown in Figure 3, the flow moves through a tortuous path and displays two regimes; namely a core flow and recirculation zones in the cavities. The core flow is a jet through flow in the leakage path which plays a dominant role in determining seal leakage. The flow recirculation zones in a cavity contribute to mechanical energy dissipation.

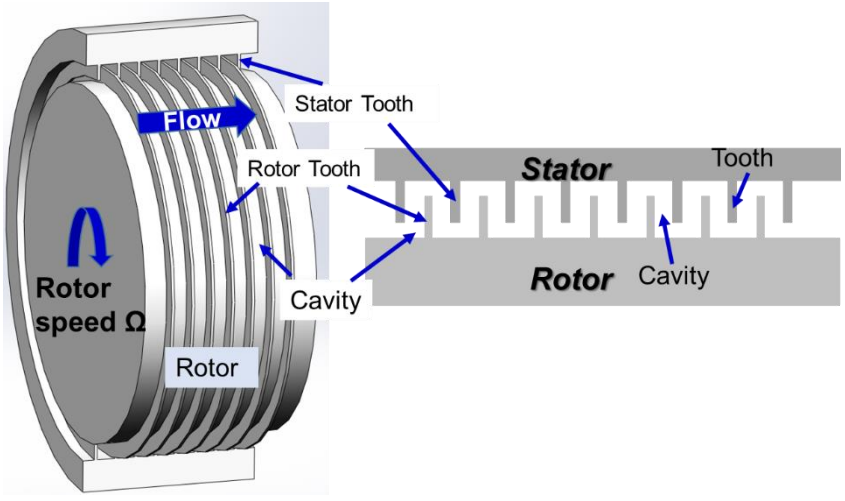

Figure 2. Interlocking labyrinth gas seal.

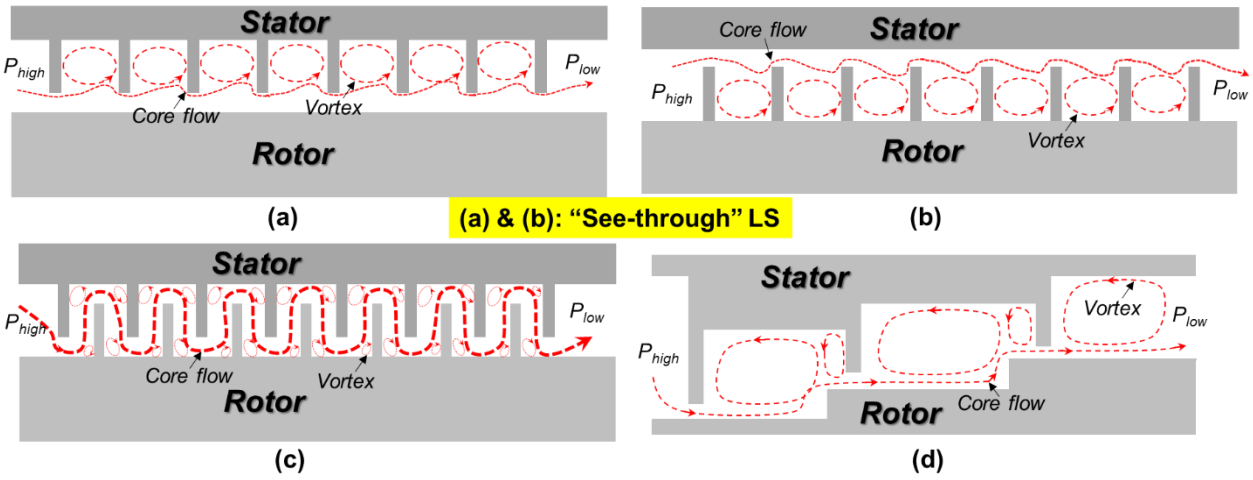

Figure 3. Schematic views of flow passing through the clearance channel in a seal: (a) TOS, (b) TOR, (c) ILS, (d) stepped LS [3].

Recently, using a CFD approach, Kuwamura et al. [3] developed a new high-performance labyrinth seal, see Figure 4. This improved LS design reduces leakage up to 30% when compared to conventional *see-through* labyrinth seals.

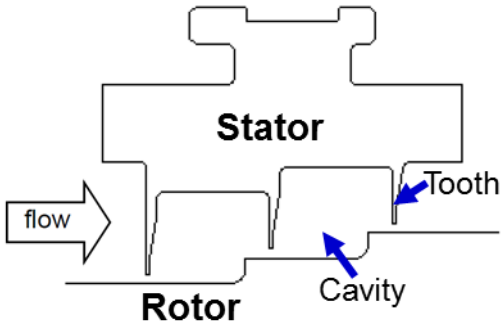

Figure 4. Schematic view of improved (stepped)labyrinth gas seal [3].

A modern compressor balance drum usually employs an interlocking labyrinth seal (ILS) to hold a high pressure drop, and thus this seal has a significant influence on rotor stability [4]. However, scant experimental results for either interlocking LSs or the stepped labyrinth seals are available.

The primary objective of the present work is to advance an accurate prediction model for LSs with correlations derived through a CFD investigation of the flow field in typical labyrinth gas seals. The CFD analysis produces a relation between kinetic energy carry-over coefficient μ_{1i} and the seal geometry (radial clearance C_r) as well as the operating conditions. Integration of the CFD

derived kinetic energy carry-over coefficient relations into the BFM contributes to an improved accuracy.

2. REVIEW OF PAST LITERATURE[3]

This review first assesses experimental works on labyrinth seals and next discusses the various numerical analyses models for labyrinth seals.

Experimental Studies on Labyrinth Seals

In 1988, Childs et al. [5] measure the leakage and force coefficients for an ILS (C_r = 0.25 mm, average tooth pitch is 5 mm, L/D = 0.34) and a TOS LS (C_r = 0.305 mm, tooth pitch is 4 mm, L/D = 0.30). The authors test the seals at a rotor speed up to 16,000 rpm (½$D\Omega$ = 126 m/s) while the supply pressure ranges from 3.0 bar to 8.0 bar ($PR = P_{in}/P_{out}$ = 3.0-8.0). The test results evidence the ILS leaks substantially less (up to 60%) than the conventional TOS LS.

In 2007, Paolillo et al. [6] demonstrate the impact of rotor speed on labyrinth seal leakage. The ratio between rotor speed ($U_{rotor} = R\Omega$) and axial flow velocity (W), U_{rotor}/W, plays an important role. When $U_{rotor}/W < 1$, rotor speed has a negligible effect on seal leakage. Li et al. [7] (2011) later confirm this finding through both experimental and numerical analyses. On the other hand, for $U_{rotor}/W > 1$, the seal leakage could significantly decrease. For large velocity ratios $U_{rotor}/W >$ 5, the seal leakage decreases more than 20% respect to that at a low velocity ratio conditions [6].

Besides rotor speed, as shown in 2008 by Gamal and Vance [8], the impact of labyrinth seal teeth thickness on seal leakage is also of interest. The authors report that doubling the teeth thickness reduces seal leakage by 10% - 20% for the test seals at all considered supply pressures (P_{in} ranges from 2 bar to 6.9 bar). As the fluid jet leaves the constriction (seal tooth), it expands into the subsequent downstream cavity. Both the clearance and the thickness of the tooth affect the angle of expansion, and therefore the amount of carried over kinetic energy [9]. Therefore, increasing the teeth thickness reduces seal leakage. Also, a thicker bladed seal may increase the frictional loss in the restriction. Test results also evidence that a reduction in cavity depth by up to 80% (the cavity depth ranges from 2.5 mm to 12.7 mm) has virtually no impact on seal leakage. The experimental and numerical analysis results from Li et al. [10] also confirm this finding.

[3] Reproduced from Ph.D. proposal of Tingcheng Wu (2018).

Analyses for Labyrinth Seals

Besides the experimental investigations, theoretical analyses for labyrinth seals are well documented since the early 1900s. In the past, researchers have produced analyses predicting the leakage and rotordynamic force coefficients of labyrinth seals. Notable to this day are the bulk-flow models (BFM) advanced by Vance and Murphy (1980) [11], Kostyuk (1972) [12], Iwatsubo et al. (1980, 1982) [13, 14], and Childs and Scharrer (1986) [15].

A BFM uses film averaged fluid pressure and flow velocities, while the wall shear stress is based on friction factors. Therefore, the BFM predictions strongly depend on the empirical coefficients, i.e., the flow discharge coefficient and the friction factor coefficients. Prior researchers have advanced several friction factor and leakage models to estimate labyrinth seal performance.

In 1908, Martin [16] considers the labyrinth to be a series of discrete throttling processes akin to the flow through a series of orifices. He derives a formula for the leakage flow through a labyrinth seal based on this model using a number of simplifying assumptions.

Later in 1935, Egli [17] examines the effect of changing the number of sharp-edged flow restrictors (teeth) and recommended that Martin's formula be used only when there are four or more throttling restrictors in series. For fewer restrictions, he used the Saint Venant-Wantzel orifice equation for each flow restriction. Egli offers test results for staggered labyrinths which show that the flow coefficient depends on the clearance and thickness of the restrictor. Later, based on Egli's [17] work, Hodkinson [9] (1939) modifies the leakage equation with a semi-empirical expression for the kinetic energy carry-over coefficient.

In 1964, Neumann [18] develops an empirical leakage formula applicable to gases and in contrast to liquids as typical orifice equations does. The formula includes a semi-empirical flow coefficient and a kinetic energy carry-over coefficient. The semi-empirical flow coefficient, accounting for the further contraction of flow after it has passed through the plane of the restrictors (teeth), is a function of the pressure ratio between the upstream and downstream cavities. The kinetic energy carry-over coefficient is determined based on the seal geometry (tooth number, radial clearance, and the seal length). In labyrinth gas seal BFM predictions, solving the Neumann's leakage equation with an iterative technique gives the leakage through a seal as well as the intermediate seal cavity pressure.

Unlike bulk-flow techniques, 3D CFD analysis makes no assumptions on the seal geometry, thus allowing (with a few million nodes) the analysis of fluid flow in an arbitrarily shaped domain, including stepped LSs and ILSs. As commercial software is readily accessible and computers processing speed continuously increase, computational fluid dynamics (CFD) analysis based approaches to solving the Navier-Stokes equations of turbulent flow in seals is (becoming) standard engineering practice.

Recently, the rapidly increased computational capacity, as well as the development of advanced algorithms (e.g., Genetic Algorithm), promote research on seal geometry optimization. In 2016, Dai et al. [19] utilize the Genetic Algorithm to identify the optimal configuration of a labyrinth seal. Multiple advanced designs are examined in detail through CFD simulations. In comparison to the baseline geometry (straight tooth see-through labyrinth seal), seals with grooves on the tooth tips show an improvement of 16% in sealing efficiency.

Rai et al. (2016) [20] utilize a 2D CFD analysis to assess the improvement in the leakage performance of a labyrinth seal and propose a new seal configuration with "air-curtains" (air injection) from the stator. The air-curtains work as fluidic barriers breaking the jet through flow in the seal leakage path. The CFD analysis evidence that implementing air-curtain in the labyrinth seal could reduce leakage by up to 50% of the conventional LS design.

Although the improvement in computational capability, 3D CFD simulations are still time-consuming and computationally expensive when compared to the BFM. For example, Migliorini et al. (2012, 2014) [21, 22] present a new CFD/Bulk-flow hybrid method to determine rotordynamic coefficients of gas seals. Briefly, the authors utilize CFD to determine the steady-state bulk-flow variables (pressure and averaged velocities across the clearance), and a bulk-flow perturbation method to obtain the reaction forces of an eccentric whirling rotor. This hybrid method predictions show better accuracy with experimental results in Ref. [23], as compared to a conventional BFM. With a computation time on the order of a typical bulk-flow analysis, the CFD/BFM hybrid method predicts rotordynamic characteristics comparable to the full 3D transient CFD analysis.

In 2018, San Andrés et al. [24] present a CFD modified BFM analysis for circumferentially shallow grooved liquid seals. Integrating the friction factors and the penetration angles in a cavity derived from CFD results into an original BFM, the authors show a significant improvement of

the BFM predictions. The BFM predictions show agreement within 14% compared to experimental estimated rotordynamic force coefficients in Ref.[25].

In 2018, Cangioli et al. [26] test a staggered labyrinth seal of diameter D=200 mm and with clearance C_r = 0.5 mm and an average tooth pitch of 3 mm. the operating conditions are rotor speed of 12,000 rpm (½$D\Omega$ = 138 m/s) and air supply pressure ranging from 64.6 bar to 91.9 bar (PR = P_{out}/P_{in} = 0.72, 0.77). Cangioli et al. [26] also modify a BFM by including the inlet (upstream) and outlet (downstream) sections for evaluation of the seal rotordynamic force coefficients calculation. The modified model shows an improved accuracy with predictions agreeing better with test results.

In 2019, Wu and San Andrés [27] presents a computational fluid dynamic (CFD) investigation quantifying the effects of labyrinth seal geometry and operating conditions on the rotor and stator circumferential friction factors ($f_{r\theta}$, $f_{s\theta}$). These are needed to improve bulk-flow model (BFM) predictions of the evolution of circumferential flow velocity and the seal force coefficients. The paper systematically studied the effects of operating conditions and seal geometry on the wall friction factors and derived new coefficients for the Blasius's friction factor model.

Recently, San Andrés et al. [28] report measurements of mass flow rate and cavity pressures for an interlocking labyrinth seal (ILS) operating over a wide range of supply and exit pressures and rotor speeds. The measurements show rotor speed has a negligible effect on the seal leakage. Both CFD and BFM predictions of leakage show a very good agreement with the test data. In this work, the authors find a unique loss coefficient for the four cavity ILS that is valid for all operating conditions.

For labyrinth seals, mechanical energy dissipation is achieved through a series of flow restrictions (teeth) and sudden expansions in the deep cavities. As the fluid accelerates through the narrow tip clearance below a sharp tooth, a fraction of its pressure (head) is converted into kinetic energy, and which is dissipated through small scale turbulence-viscosity interaction in the immediate cavity downstream. To estimate the mass flow rate in a LS engineering analyses use Neumann's [18] formula, $\dot{m}_i = \mu_{1i}\mu_{2i}\left(\pi D C_r\right)\sqrt{P_{i-1}^2 - P_i^2/R_gT}$, $i = 1,2,\cdots$, an orifice like equation relating flow to pressure drop, and that uses a flow coefficient (μ_{2i})and a kinetic energy carry-over (μ_{1i}) coefficient [29]. For both TOS LS and TOR LS, $\mu_{1i} = \sqrt{NT/[(1-\lambda)NT + \lambda]}$, $\lambda = 1-\left(1+16.6\, C_r/L_i\right)^{-2}$ depends on the seal clearance C_r, cavity width or tooth pitch L_i, and total teeth number NT; whereas, μ_{1i} = 1 in an ILS [29].

For a LS having a large C_r/L_i ratio, simple bulk-flow model (BFM) could not accurately predict the mass flow rate. Thus, better assessing the kinetic energy carry-over coefficient in a LS is of great significance to improve BFM leakage predictions, and a modification of the bulk-flow model with CFD derived results could be a practical way.

3. PREDICTION OF ROTORDYNAMIC FORCE COEFFICIENTS FOR LABYRINTH GAS SEALS[4]

Governing Equations

In 1986, Childs and Scharrer [15], based on Iwatsubo's early model [13, 14], derive the equations of a one control volume bulk flow model applied to a labyrinth seal. The following update follows the original derivation. Figure 5 shows schematic views of an ILS with radial clearance C_r and rotor radius R_s. Teeth on both the rotor and the stator have the same geometry, with B as a tooth height and L_i as a tooth pitch.

The flow domain is divided into n cavities separated by blades. As Figure 6 shows, within the i^{th} cavity, the pressure is P_i, and the mean circumferential velocity is U_i. The velocity U_i differs from one cavity to the next, but it is sufficiently uniform in a single cavity to permit its bulk flow representation. The mass flow rate through the upstream and downstream teeth is $\dot{m}_i=\dot{m}_{i+1}$.

The gas density (ρ) follows the ideal gas law, $\rho=P/(Z_gR_gT)$, where R_g and Z_g are the gas constant and compressibility factor, and T is the gas temperature[5]. Figure 7 depicts the forces on a control volume, serving to derive the circumferential momentum equation.

In a cavity, the flow mass conservation equation and momentum transport equation along the circumferential (θ) direction are [15]:

$$\frac{\partial(\rho_i A_i)}{\partial t}+\frac{\partial(\rho_i U_i A_i)}{R_s\ \partial\theta}+\dot{\bar{m}}_{i+1}-\dot{\bar{m}}_i=0 \tag{2}$$

$$\frac{\partial(\rho_i U_i A_i)}{\partial t}+\frac{\partial(\rho_i A_i U_i^{\,2})}{R_s\ \partial\theta}=-\frac{A_i}{R_s}\frac{\partial P_i}{\partial\theta}+(\tau_{r_i}a_{r_i}-\tau_{s_i}a_{s_i})L_i \tag{3}$$

where $A_i=(B+C_r)L_i$ is the area of a cavity cross-section.

[4] Reproduced from Ph.D. proposal of Tingcheng Wu (2018).

[5] Since experimental investigations do not show a significant temperature change throughout typical seals, the model assumes isothermal flow conditions [5].

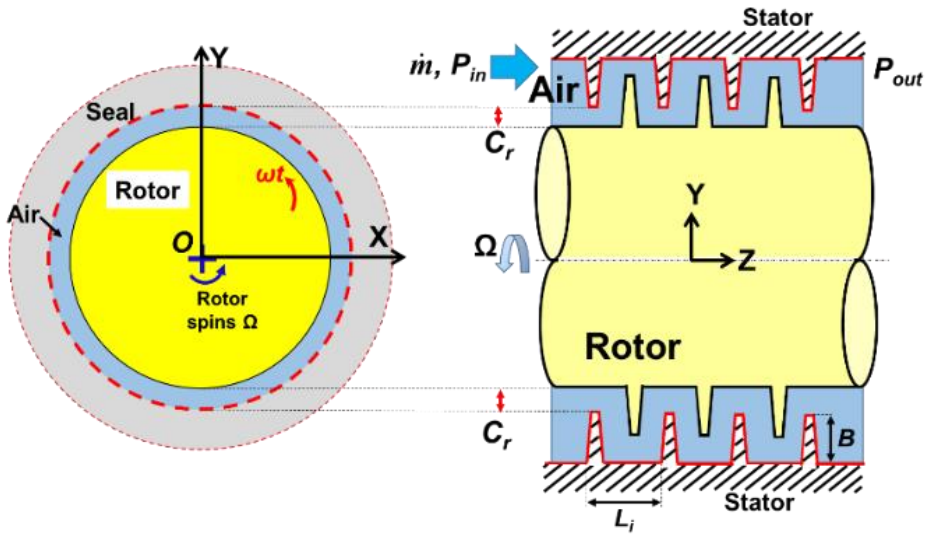

Figure 5. Schematic view (not to scale) of an interlocking labyrinth seal (ILS).

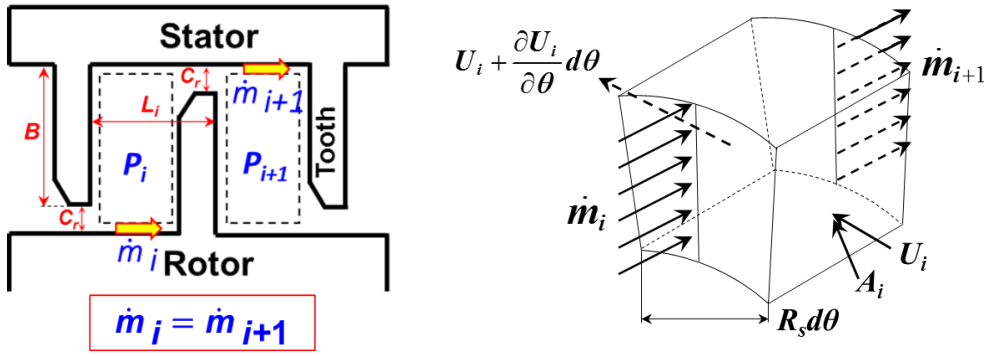

Figure 6. Schematic views of a one-control-volume model (*i* = the cavity number).

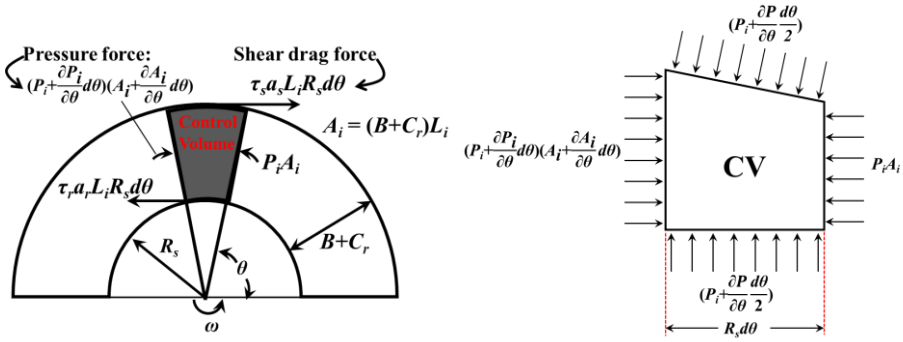

Figure 7. Forces on the control volume of a labyrinth seal (*i* = the cavity number).

Using Neumann's equation [2] that relates the mass flow rate ($\dot{m}$) through a tooth clearance (C_r) as a function of the upstream (P_{i-1}) and downstream (P_i) cavity pressures,

$$\bar{\dot{m}}_i\left(\pi D\right)=\dot{m}_i=\mu_{1i}\mu_{2i}\left(\pi DC_r\right)\sqrt{\frac{P_{i-1}^2-P_i^2}{R_gT}},\ i=1,2,\cdots,N \tag{4}$$

where, μ_{1i} is a kinetic energy carry-over coefficient, and μ_{2i} is a flow discharge coefficient, see Ref. [2].

For a *see-through* labyrinth seal (TOR or TOS) with diameter *D*, the Neumann's empirical leakage equation (Eqn. (4)) with Chaplygin's [30] flow coefficient (μ_{2i}) predicts the gas leakage ($\dot{m}$) across a seal tooth with tip clearance C_r [2, 31]. For a *see-through* (TOR a TOS) labyrinth seal, the kinetic energy carry-over coefficient (μ_{1i}) is a function of the seal geometry

$$\mu_{1i}=\left(\frac{NT}{\left(1-\lambda\right)NT+\lambda}\right)^{\frac{1}{2}} \tag{5}$$

$$\lambda=1-\left(1+16.6\ C_r/L_i\right)^{-2} \tag{6}$$

For the first tooth in a see-through LS and all the teeth in an ILS, μ_{1i} equals unity [2]. Note λ is constant in a seal with uniform teeth spacing (cavity widths and depth).

Consider as an example a TOS LS with seven teeth, C_r = 0.2 mm and L_i = 5 mm, C_r/L_i = 0.04; and Figure 8(a) thus shows the change of μ_1 with respect to the ratio C_r/L_i. μ_1 increases monotonically with C_r/L_i, starts at a magnitude of one and approaches to a maximum value ~2.6.

The flow discharge coefficient μ_{2i} uses Chaplygin's formula, Gurevich (1966) [2, 31] and equals

$$\mu_{2i}=\frac{\pi}{\pi+2-5\beta_i+2\beta_i^2} \tag{7}$$

with

$$\beta_i=\left(\frac{P_{i-1}}{P_i}\right)^{\frac{\gamma-1}{\gamma}}-1 \tag{8}$$

where γ is the ratio of specific heats. For air, γ=1.4. Figure 8(b) shows the change of μ_2 with respect to the pressure ratio (P_{i-1}/P_i). Note μ_2 is proportional to the increase in cavity pressures (upstream/downstream). Prior to the flow choking across a tooth, the largest (P_{i-1}/P_i) is, the higher μ_2 becomes.

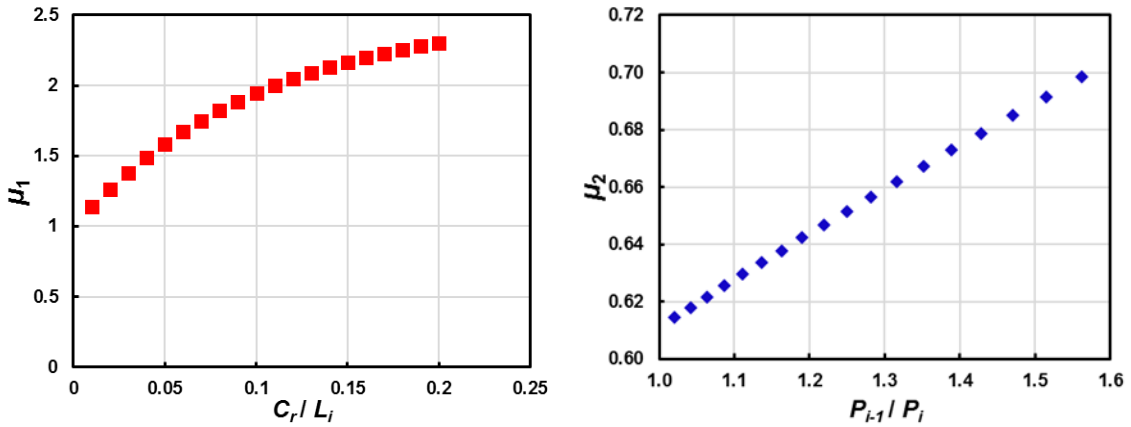

(a) μ_1 vs. C_r/L_i **(b) μ_2 vs. (P_{i-1}/P_i)**

Figure 8. A sample see-through labyrinth seal with seven teeth: (a) variation of kinetic energy carry-over coefficient μ_1 vs. C_r/L_i; and (b) flow discharge coefficient μ_2 vs. (P_{i-1}/P_i) : cavity pressures upstream/downstream.

Flow Perturbation Analysis

For the i^{th} cavity, the continuity equation (1), circumferential momentum equation (2) and leakage equation (3) are the governing equations for the variables U_i, P_i, and m_i. For small amplitude rotor motions ($\Delta e_x, \Delta e_y$) of frequency ω, the film thickness (H) as depicted in Figure 9 is

$$H = C_r + e^{j\omega t}(\Delta e_x \cos\theta + \Delta e_y \sin\theta) \tag{9}$$

The velocity and pressure fields are expressed as the sum of a zeroth order and first order complex fields, describing the equilibrium condition and the perturbed motions, i.e.

$$\phi = \phi\{P, U, W\} = \phi_0 + e^{jwt}(\Delta e_x \ \phi_x + \Delta e_y \ \phi_y),\ j = \sqrt{-1} \tag{10}$$

Substitution of the flow variables into the governing equations yields the differential equations for the zeroth and first-order flow fields.

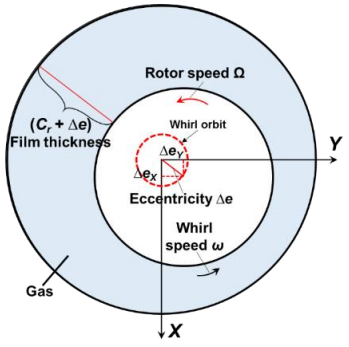

Figure 9. Depiction of small amplitude rotor motions about a centered position.

The zeroth order flow equations

$$\bar{\dot{m}}_0 = \bar{\dot{m}}_i = \bar{\dot{m}}_{i+1} \ , \ i = 1,2,3,\ldots \tag{11}$$

$$\bar{\dot{m}}_0 (U_{0i} - U_{0i-1}) = (\tau_{r0i} a_{r_i} - \tau_{s0i} a_{s_i}) L_i \tag{12}$$

determine the mass flow rate $\dot{m}_0$, cavity pressures (P_{i0}), and velocity field ($U_{i0,}$ i=1,2,..) for the rotor centered position. First-order equations are not detailed for brevity.

Childs [29] details the procedure to solve the partial differential equations governing the fluid flow. The perturbation analysis renders the seal static and dynamic reaction forces as

$$-\begin{bmatrix} F_{X(\omega)} \\ F_{Y(\omega)} \end{bmatrix} = -\begin{bmatrix} F_{X0} \\ F_{Y0} \end{bmatrix} + \begin{bmatrix} D_{(\omega)} & E_{(\omega)} \\ G_{(\omega)} & F_{(\omega)} \end{bmatrix} \begin{bmatrix} X_{(\omega)} \\ Y_{(\omega)} \end{bmatrix} \tag{13}$$

The functions *D*-*F* are frequency-dependent and obtained as

$$\begin{bmatrix} D \\ G \end{bmatrix}_{(\omega)} = R_s \int_0^L \int_0^{2\pi} P_X \begin{bmatrix} \cos\theta \\ \sin\theta \end{bmatrix} d\theta \, dz; \begin{bmatrix} E \\ F \end{bmatrix}_{(\omega)} = R_s \int_0^L \int_0^{2\pi} P_Y \begin{bmatrix} \cos\theta \\ \sin\theta \end{bmatrix} d\theta \, dz \tag{14}$$

Note that for motions about a centered rotor position, $D = F$, $E = -G$. Stiffness and damping coefficients follow from

$$K_{(\omega)} + j\,\omega C_{(\omega)} \leftarrow D_{(\omega)}; \; k_{(\omega)} + j\,\omega c_{(\omega)} \leftarrow E_{(\omega)} \tag{15}$$

The BFM analysis procedure is well documented in Refs. [15, 29, 32]. In brief, the BFM solution procedure follows the steps:

(1) Determine whether the flow is choked or not by comparing the inlet pressure against the critical inlet pressure (as discussed later);

(2) Calculate the mass flow rate, cavity pressure distribution and the cavity circumferential velocity.

(3) Solve the first order (perturbed) equations for a given whirl frequency (ω), integrate the dynamic pressure acting on the rotor surface to calculate the reaction forces, and thus obtaining the rotordynamic force coefficients.

4. CFD ANALYSIS PROCEDURE

The TOS seal geometry and its operating conditions applied in this work are based on a TOS labyrinth seal tested by Vannini et al. (2014) [33]. Table 1 details the TOS labyrinth seal geometry and operating parameters. Figure 10 shows a schematic view of the TOS labyrinth seal, having 14 teeth on the stator. The teeth are equally distributed with pitch length L_i of 5 mm. To investigate

the effect of seal geometry and operating conditions on the friction factors, the seal clearance varies from $0.8C_r$ to $2C_r$. Similarly, perturbations also apply to the seal operating conditions. For all TOS labyrinth seals (various radial clearances), the rotor speed is 12,000 rpm. Air enters the seal with supply pressure P_{in} = 60, 73, 100 bar (absolute) and room temperature (27 °C). The seal outlet the exit pressure (P_{out}) is set to determine a pressure ratio ($PR = P_{out}/P_{in}$) ranging from 0.4 to 0.85.

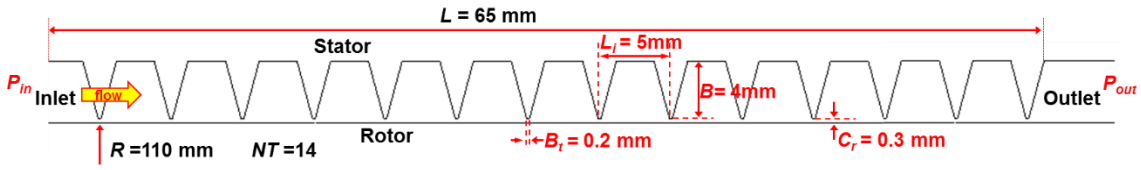

Figure 10. Schematic view of TOS labyrinth gas seal in Ref. [33].

Table 1. Dimensions and operating conditions of the teeth-on-stator (TOS) labyrinth seal in Ref. [33].

Seal Geometry	Seal length, L	65 mm
	Rotor diameter, D	220 mm
	Radial clearance, C_r	0.3 mm
	Teeth number, NT	14
	Tooth pitch, L_i	5 mm
	Height, B	4 mm
	Width at tip, b_t	0.2 mm
Air Properties (ideal gas)	Density, ρ @1bar	1.28 kg/m^3
	Temperature, T	300 K
	Sound speed, V_s	314 m/s
	Viscosity, v	1.51×10^{-5} m^2/s
Operating Conditions	Supply pressure, P_{in}	60 bar ~ 100 bar
	Discharge pressure, P_{out}	40 bar ~ 70 bar
	Pressure ratio, $PR= P_{out}/P_{in}$	0.40 ~ 0.85
	Pre-swirl velocity, U_0	0
	Rotor Speed, Ω	12 krpm
	($R\Omega$)	(138 m/s)

Figure 11 shows the computational domain and corresponding mesh for the TOS labyrinth seal with nominal radial clearance. 15 mm in length extensions at the seal upstream and downstream flow sections capture the flow field before and after the seal section, respectively. Various mesh sets, their total node count ranging from 2.8 million to 10 million, serve to conduct a mesh independence analysis, see Table 2. The grid independence analysis is not discussed here for

simplicity. The grid independence test indicates a mesh with 8.7 million nodes is sufficient to capture the flow field characteristics.

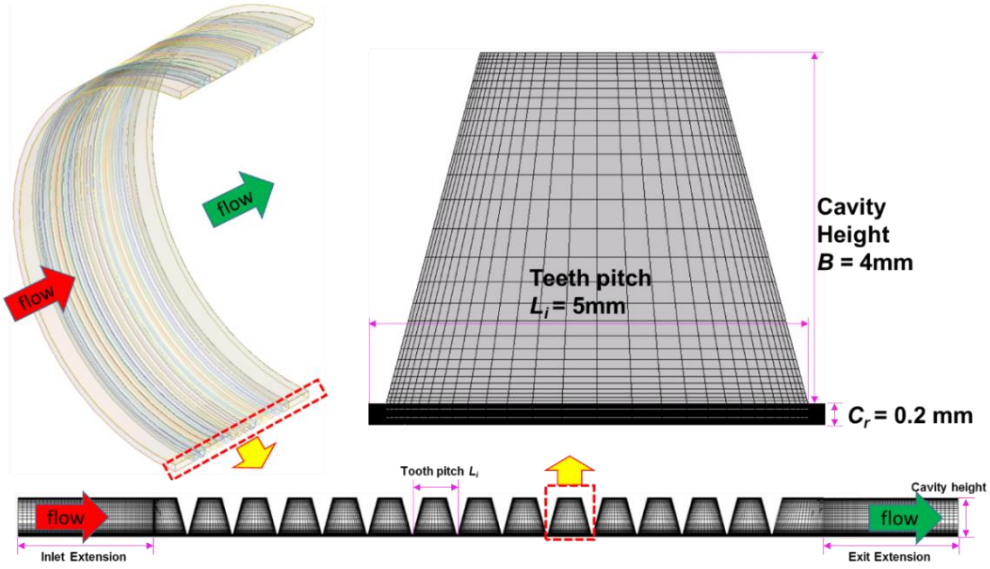

Figure 11. CFD mesh for a TOS labyrinth gas seal.

Table 2. Details of mesh distribution for model labyrinth seals.

	Node number/ mesh size
Radial clearance	30
Tooth section	30
Cavity depth/length	30
Circumferential	180 (2° apart)
Min. mesh orthogonal quality	0.99

5. BFM AND CFD PREDICTED MASS FLOW RATE

Note the procedure to calculate the seal mass flow rate as well as the cavity pressures is well documented in a prior(2017) TRC report [34]; henceforth not discussed here.

For a compressible fluid, the density (ρ) is a function of the local pressure, thus varying from cavity to cavity. From the seal inlet plane towards the outlet plane, the circumferential flow velocity develops. Recall, the BFM assumes the cavity pressure (and density), and the circumferential velocity are constant within a cavity. Therefore, all the variables extracted from CFD results in a representative analysis should correspond to an average across the cavity width and radial depth.

Figure 12(a) shows the contours of density along the seal. The density within a cavity (#1-#13) is almost uniform; and so does the tangential velocity in (b). Figure 12 (c) and (d) depict from the seal inlet plane to the outlet plane the cross-film average (normalized) density (ρ/ρ_s) and the cross-

film average (normalized) circumferential velocity (U/U_{rotor}, $U_{rotor} = R\Omega$). The cavity density (and pressure) shows a linear drop from the seal inlet plane toward the outlet plane whereas the fluid tangential velocity in a cavity grows towards the seal discharge. Recall a null pre-swirl condition is applied and the seal is short in length ($L/D = 0.3 < 0.5$); hence the fluid mean circumferential velocity in the last cavity is less than $\frac{1}{2}D\Omega$.

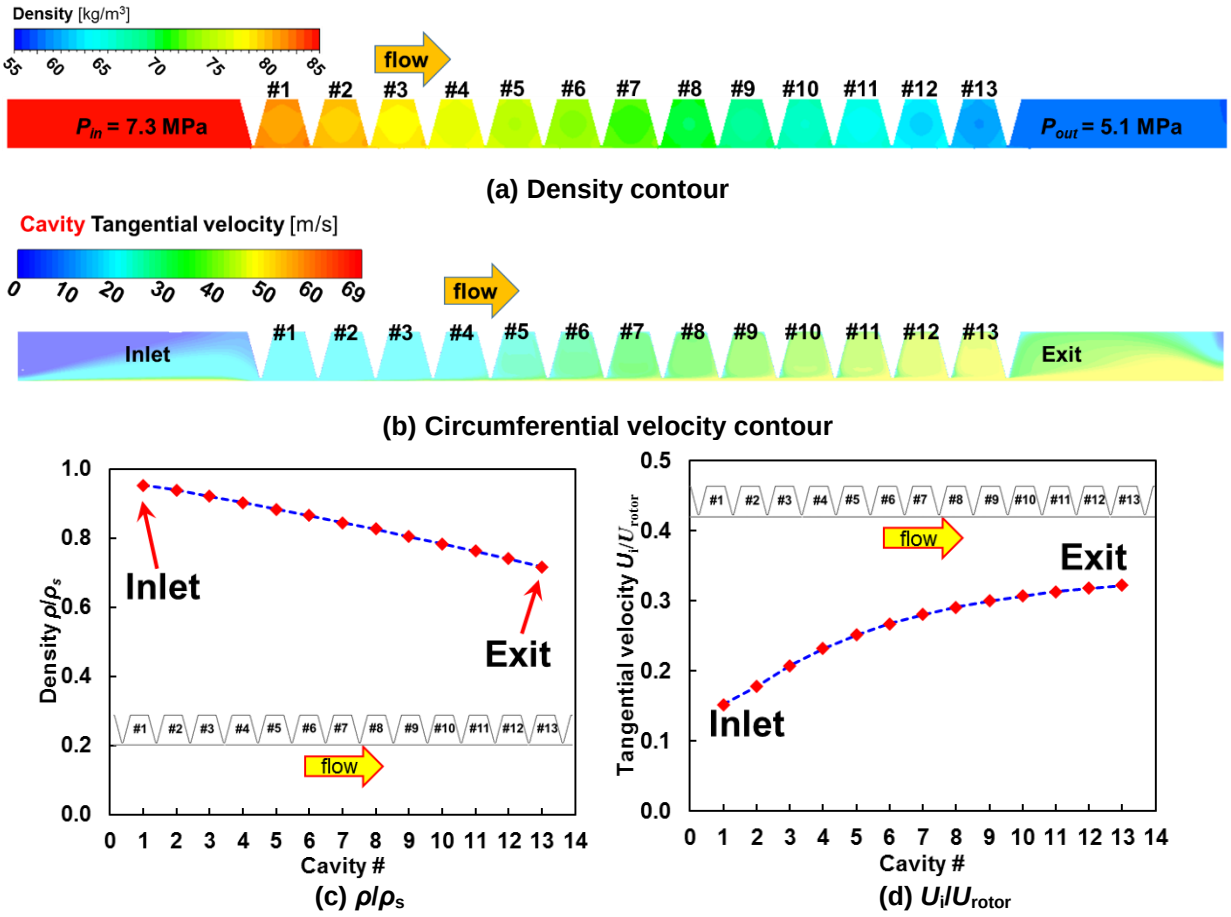

Figure 12. CFD predictions for a TOS LS: (a) density contours; (b) circumferential velocity contours; (c) cross-film averaged cavity density (ρ/ρ_s); (d) cross-film averaged tangential velocity (U_i/U_{rotor}) within a cavity. P_{in} = 7.3 MPa, P_{out} = 5.1 MPa, rotor speed = 12 krpm (138 m/s).

In engineering practice, the seal radial clearance C_r ranges from 3~5‰ of the rotor radius and increases after a period of operation due to the wear. In this study, the seal has a nominal radial clearance C_r = 3‰×R, and cases with up to 2×C_r (6‰×R) are included to account for seal wear conditions. Table 3 lists the TOS labyrinth seal mass flow rate predicted by both the CFD and BFM methods. As the seal radial clearance varies from 80% to 200% of the nominal size (C_r =

0.3mm), the current BFM under-estimates the mass flow rate by 6.9%~18.9%. The supply pressure P_{in} increases from 60 bar to 100 bar, where the pressure ratio $PR = P_{out}/P_{in}$ = 0.4 ~0.85, and the rotor speed is 12 krpm ($R\Omega$ = 138 m/s).

For all the operating conditions herein considered, the discrepancy between BFM and CFD predictions ranges from 1.5% to 18.9%. The seal with $2\times C_r$ shows the maximum difference (18.9%) between the CFD and BFM predicted mass flow rates. When the supply pressure is fixed, the discrepancy between CFD and BFM predicted mass flow rates increases with respect to the pressure ratio *PR*. On the other hand, for a fixed *PR*, the larger the supply pressure P_{in}, the more different the BFM predicted mass flow rate becomes when compared to the CFD prediction.

Table 3. CFD and BFM predicted mass flow rate of TOS labyrinth seals, seal radial clearance = (0.8, 1.0, 1.2, 2.0) ×C_r, supply pressure increases from 60 to 100 bar, pressure ratio $PR = P_{out}/P_{in}$ = 0.4 ~ 0.85, and rotor speed Ω = 12 krpm ($R\Omega$ = 138 m/s).

Operating Conditions	Prediction Method	Mass Flow Rate [kg/s]			
		0.8 × Cr	1.0 × Cr	1.2 × Cr	2.0 × Cr
P_{in}=60 bar, *PR* = 0.85	CFD	0.495	0.606	0.865	1.868
	BFM	0.460	0.615	0.781	1.515
	Diff.	**-6.9%**	**1.5%**	**-9.7%**	**-18.9%**
P_{in} =72.8 bar, *PR* = 0.7	CFD	0.835	1.123	1.446	3.081
	BFM	0.760	1.017	1.291	2.509
	Diff.	**-8.9%**	**-9.5%**	**-10.7%**	**-18.5%**
P_{in} =100 bar, *PR* = 0.4	CFD	1.465	1.960	2.525	5.181
	BFM	1.355	1.811	2.303	4.485
	Diff.	**-7.5%**	**-7.6%**	**-8.8%**	**-13.4%**
P_{in} =100 bar, *PR* = 0.5	CFD	1.387	1.859	2.397	4.964
	BFM	1.274	1.702	2.163	4.205
	Diff.	**-8.1%**	**-8.4%**	**-9.8%**	**-15.3%**
P_{in} =100 bar, *PR* = 0.7	CFD	1.153	1.550	2.000	4.246
	BFM	1.045	1.397	1.774	3.447
	Diff.	**-9.4%**	**-9.9%**	**-11.3%**	**-18.8%**

Figure 13(a) depicts both the CFD and BFM mass flow rates versus pressure ratio (*PR*). The lows are normalized with respect to the ones obtained for the nominal clearance ($1\times C_r$). For a large C_r (>1), the discrepancy between CFD and BFM predictions grows larger.

The flow factor $\phi = \dot{m}\sqrt{T}/(P_{in}D)$ introduced by Delgado and Proctor [35] serves to quantify the leakage of gas seals in a manner that shows independence of the seal size (diameter *D*) and inlet flow conditions, namely pressure (P_{in}) and temperature (*T*). Figure 13(b) shows the flow factor (

$\phi = \dot{m}\sqrt{T}/(D \cdot P_{in})$) versus pressure ratio (*PR*) for both CFD and BFM predictions. The flow factor ϕ decreases with respect to an increase in *PR*, the difference between CFD and BFM predictions increases with an increase in C_r. Therefore, the effects of seal radial clearance C_r and the operating pressure ratio *PR* should be considered in the modification of flow equations.

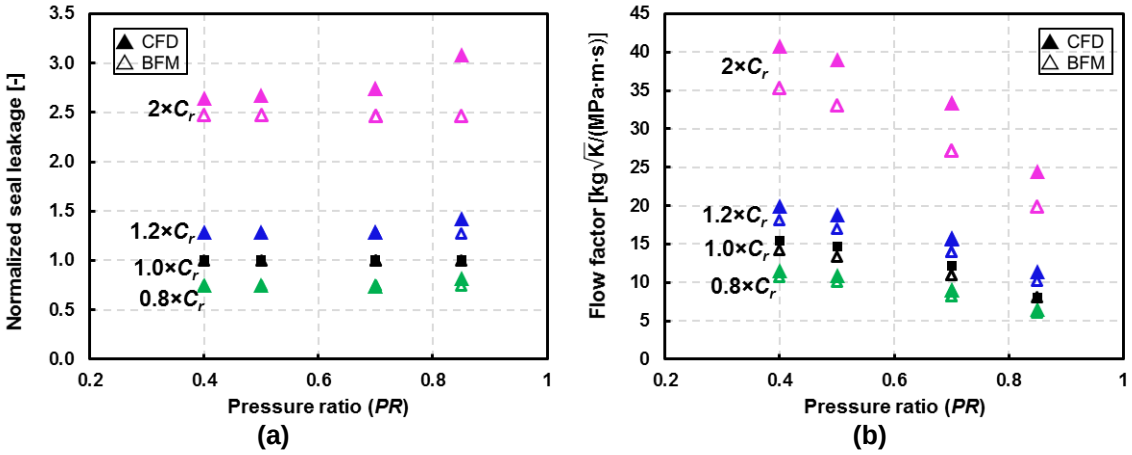

Figure 13. CFD and BFM predicted (a) normalized mass flow rate vs. *PR*; (b) flow factor vs. *PR*. TOS labyrinth seal, radial clearance = (0.8, 1.0, 1.2, 2.0) ×C_r, supply pressure increases from 60 to 100 bar, pressure ratio *PR*= P_{out}/P_{in} = 0.4 ~ 0.85, and rotor speed Ω = 12 krpm (*R*Ω = 138 m/s).

San Andrés et al. [28] introduce a modified flow factor

$$\bar{\Phi} = \frac{\phi}{\sqrt{1-PR^2}} = \frac{\dot{m}\sqrt{T}}{D\,P_{in}\sqrt{1-PR^2}} \sim \pi\ c_d\, C_r \frac{1}{\sqrt{R_g}} \tag{16}$$

which can easily lead to the determination of a seal loss coefficient c_d, or as in some cases, the definition of an effective clearance ($C_{eff} = c_d \times C_r$), both representing the seal effectiveness to reduce leakage. Figure 14 depicts the modified flow factor ($\bar{\Phi}$) versus pressure ratio and the various clearances considered. $\bar{\Phi}$ increases with respect to an increase in seal radial clearance C_r; whereas for a fixed C_r, $\bar{\Phi}$ remains almost constant as *PR* varies from 0.4 to 0.85. On the other hand, the flow coefficient $c_d = C_{eff}/C_r$, the lowest magnitude desired to make more effective the seal resistance to leakage, increases with respect to the physical clearance magnitude.

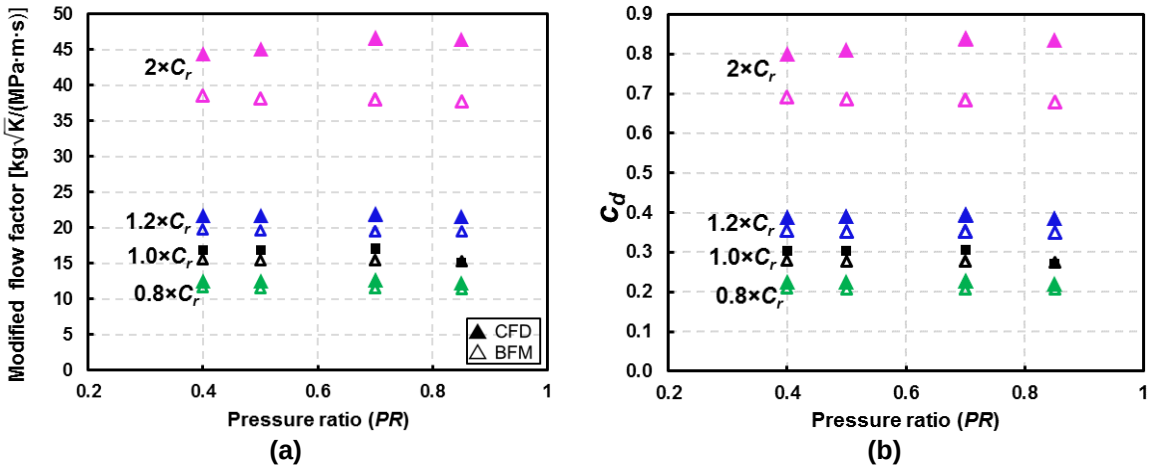

Figure 14. CFD and BFM predicted modified flow factor (Φ) and flow coefficient (c_d) vs. seal $PR = P_{out}/P_{in}$. TOS labyrinth seal, radial clearance = (0.8, 1.0, 1.2, 2.0) ×C_r. Supply pressure varies from 60 to 100 bar and rotor speed Ω = 12 krpm ($R\Omega$ = 138 m/s).

6. MODIFIED LEAKAGE PREDICTION MODEL

Figure 15 depicts the CFD predicted cavity pressure (P_i/P_{in}) vs. cavity number for seals with different operating pressures. The flow passes through the upstream cavity and suffers a sudden flow contraction at the first seal tooth. Therefore, the flow velocity increases and so does the kinetic energy. As a result, the first cavity pressure has a sudden drop.

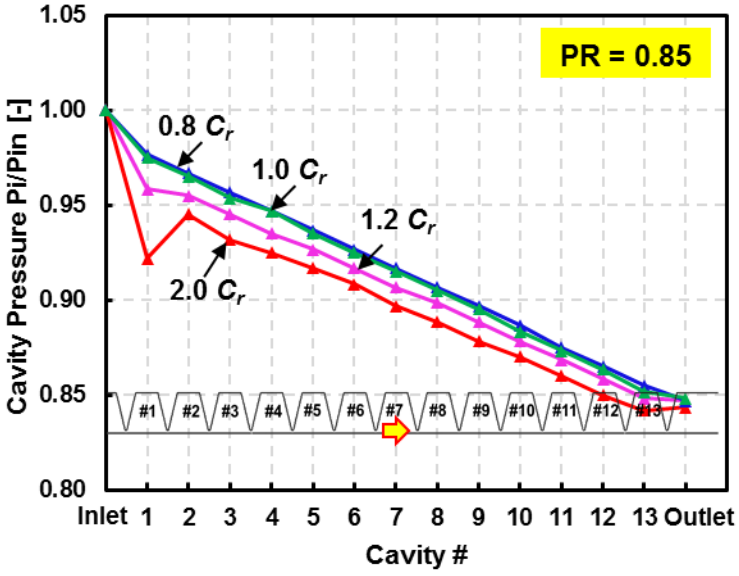

(a) P_{in} = 60 bar, PR = 0.85

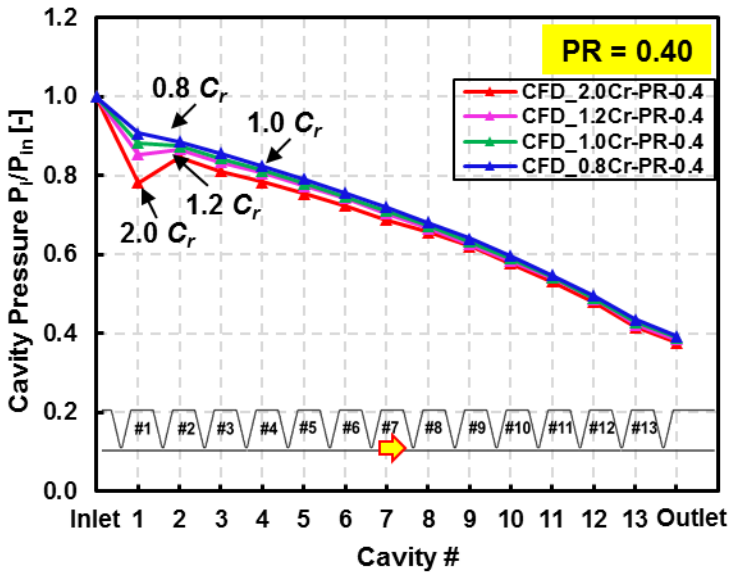

(b) P_{in} = 100 bar, PR = 0.4

Figure 15. CFD predicted cavity pressure (P_i/P_{in}) vs. cavity #. TOS labyrinth seal with radial clearance ranging from 0.8×C_r to 2.0 ×C_r, rotor speed Ω = 12 krpm ($R\Omega$ = 138 m/s). (a) supply pressure P_{in} = 60 bar, pressure ratio PR = 0.85; (b) supply pressure P_{in} = 100 bar, pressure ratio PR = 0.40.

Figure 16(a) depicts the flow velocity contours for the TOS labyrinth seals with 1×C_r and 2×C_r. As the flow enters the seal, the larger the radial clearance is, the higher the increase in flow velocity. Therefore, for the seal with a larger radial clearance, the first cavity pressure drops more than the TOS labyrinth seal with a smaller clearance. On the other hand, as the seal radial clearance increases, the first cavity develops a stronger vortex with respect to C_r, which later contributes to the static pressure recovery in the second cavity. The second cavity flow velocity shows a decrease compared to that in the first cavity. Figure 16(b) depicts the normalized cavity velocity, as referenced to that in the first cavity, i.e. (V_i/V_1). For all the operating conditions considered hereby, the second cavity velocity shows a decrease, which could explain the second cavity static pressure recovery shown in Figure 15. For a fixed clearance, the percentage of the decrease in second cavity velocity is a function of the pressure ratio PR only; the smallest PR produces the maximum velocity decrease in terms of percentage. For a fixed supply pressure P_{in}, the cavity flow velocity develops faster for the case with a lower pressure ratio PR. For a fixed pressure ratio PR, a larger supply pressure leads to a slower cavity velocity development.

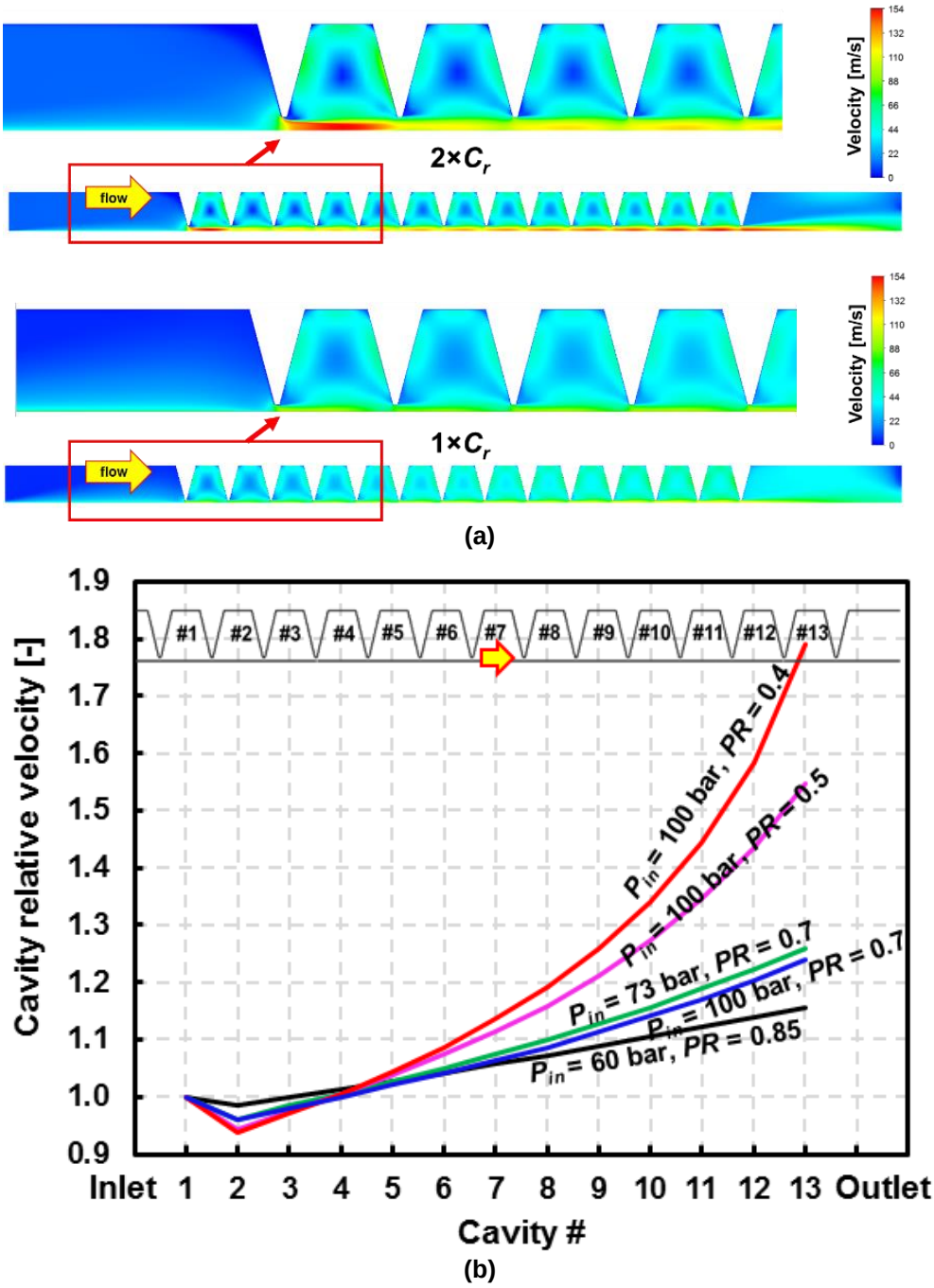

Figure 16. CFD predicted cavity velocity vs. cavity #. TOS labyrinth seal with (a) radial clearance = 1×C_r and 2.0 ×C_r, supply pressure P_{in} = 100 bar, pressure ratio PR = 0.7; (b) radial clearance = 2.0×C_r, supply pressure P_{in} = 60 bar, 73 bar, 100 bar, pressure ratio PR = 0.40, 0.5, 0.7, 0.85. Rotor speed Ω = 12 krpm (RΩ = 138 m/s).

Figure 17 depicts the CFD and BFM predicted cavity pressure distribution vs. cavity number. The current BFM model could not accurately calculate the pressure drop across the first tooth

which is significantly lower than the CFD prediction. The discrepancy increases with an increase in the seal radial clearance.

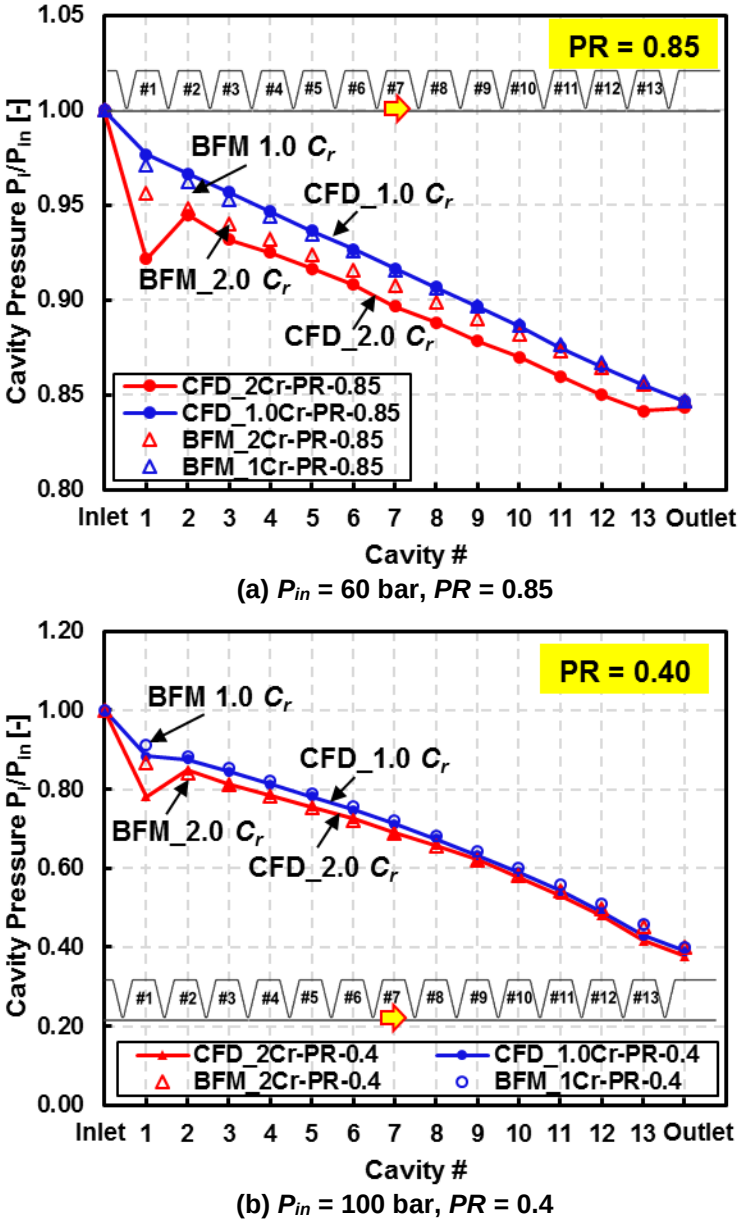

Figure 17. CFD and BFM predicted cavity pressure (P_i/P_{in}) vs. cavity #. TOS labyrinth seal with radial clearance = 1.0×C_r and 2.0 ×C_r, rotor speed Ω = 12 krpm. (a) supply pressure P_{in} = 60 bar, pressure ratio PR = 0.85; (b) supply pressure P_{in} = 100 bar, pressure ratio PR = 0.40.

Recall that the BFM utilizes Neumann's Eqn. (4) to calculate the seal leakage as well as the cavity pressure distribution. In Eqn. (4), the flow discharge coefficient μ_{2i} is a function of the cavity pressure distribution, whereas the kinetic energy carry-over coefficient (μ_{1i}) is a function of the

seal geometry (radial clearance C_r and tooth pitch L_i). Recall, μ_{1i} for the first tooth of a labyrinth seal is unity. One should note that the current leakage model does not take the effect of pressure ratio (*PR*) into consideration, while the above analysis shows the cavity pressure distribution is a function of the pressure ratio, particularly at the first cavity.

With the CFD predicted mass flow rate and cavity pressures, one could calculate the flow discharge coefficient μ_{2i} for each tooth, and therefore deriving the corresponding kinetic energy carry-over coefficient μ_{1i}. Table 4 lists the kinetic energy carry-over coefficient μ_{1i} derived from CFD predictions and calculated from

$$\mu_{1i} = \frac{\dot{m}_i}{\left(\mu_{2i} \left(\pi D C_r \right) \sqrt{\dfrac{P_{i-1}^2 - P_i^2}{R_g T}} \right)}, \; i = 1, 2, \cdots, N \tag{17}$$

and the μ_{1i} in the original Neumann equations, i.e. Eqns. (5) and (6), or $\mu_{1i} = \sqrt{NT/\left((1-\lambda)NT + \lambda\right)}$ with $\lambda = 1 - \left(1 + 16.6\, C_r / L_i\right)^{-2}$). One should note that for those cases with a strong first cavity pressure drop and a second cavity pressure recovery, $P_1 < P_2$. Thus, $(P_1^2 - P_2^2) < 0$ and from Eq. (4), $\mu_{12} \sim \dot{m}_2 \Big/ \left(\sqrt{P_1^2 - P_2^2} \right)$ at the second tooth has no meaning as it would be an imaginary number. That is, the CFD predicted kinetic energy carry-over coefficient for the second tooth (μ_{12}) could not be calculated. On the other hand, the pressure drop ($\Delta P_{14} = P_{13} - P_{14}$) across the last tooth is relatively smaller than that across other teeth; hence a lower μ_2 which produces the unusual jump in μ_1, as seen in the last row in Table 4.

Different from the CFD simulations, the BFM cannot capture flow details within a cavity, neither the pressure recovery occurring in the second cavity. The CFD predicted cavity pressure distribution indicates that the pressure drop along the axial direction is not strictly linear. Thus, the CFD derived μ_{1i} varies from cavity to cavity, see Table 4. In order to adequately account the pressure variations as predicted by CFD simulations, μ_{1i} is obtained from an average of the CFD predictions listed in Table 5, though excluding the values obtained at the first and last teeth. The original Eqns. (5) and (6) underestimate the kinetic energy carry-over coefficient μ_{1i} by up to 52% when compared to the CFD predictions.

Table 4. Kinetic energy carry-over coefficient μ_{1i} derived from CFD predictions. TOS labyrinth seal with radial clearance = (0.8, 1.0, 1.2, 2.0) ×C_r, supply pressure P_{in} = 100 bar, pressure ratio $PR = P_{out}/P_{in}$ = 0.4, and rotor speed Ω = 12 krpm ($R\Omega$ = 138 m/s).

Tooth #	0.8C_r -100bar-PR0.4	1C_r -100bar- PR0.4	1.2C_r -100bar- PR0.4	2C_r -100bar- PR0.4
1	0.98	0.93	0.89	0.89
2	2.16	3.80	**N/A**	**N/A**
3	1.83	1.94	2.02	2.41
4	1.80	1.94	2.24	2.85
5	1.83	1.98	2.10	2.75
6	1.76	1.96	2.21	2.75
7	1.80	1.94	2.01	2.65
8	1.78	1.97	2.15	2.88
9	1.80	1.92	2.07	2.70
10	1.77	1.93	2.11	2.55
11	1.74	1.91	2.16	2.61
12	1.76	1.88	2.00	2.53
13	1.70	1.84	1.91	2.39
14	2.20	2.49	2.73	3.30
Eq. (5)	1.67	1.81	1.95	2.39

Table 5. Updated kinetic energy carry-over coefficient μ_{1i} derived from average CFD predictions (Table 4). TOS labyrinth seal with radial clearance = (0.8, 1.0, 1.2, 2.0) ×C_r, supply pressure P_{in} = 60 ~ 100 bar, pressure ratio $PR = P_{out}/P_{in}$ ranges from 0.4 to 0.85, and rotor speed Ω = 12 krpm ($R\Omega$ = 138 m/s).

Operating Conditions	New μ_{1i} (i = 2, 3, …, NT)			
	0.8 × Cr	**1.0 × Cr**	**1.2 × Cr**	**2.0 × Cr**
P_{in} =60 bar, PR = 0.85	1.80	1.76	2.20	3.11
P_{in} =72.8 bar, PR = 0.7	1.89	2.06	2.28	3.27
P_{in} =100 bar, PR = 0.4	1.84	2.01	2.20	2.96
P_{in} =100 bar, PR = 0.5	1.85	2.03	2.24	3.06
P_{in} =100 bar, PR = 0.7	1.90	2.08	2.30	3.30
Original Eqn. (5)	1.67	1.81	1.95	2.39

Figure 18 illustrates the updated μ_{1i} (listed in Table 5) vs. radial clearance for seals operating with various pressure ratios (PR). In general, the new μ_{1i} increases linearly with respect to the seal radial clearance. On the other hand, the new μ_{1i} shows a non-linear correlation with the pressure ratio PR.

Towards delivering more accurate mass flow rate predictions, a modified kinetic energy carry-over coefficient model considers the effect of pressure ratio PR as

$$\mu_{1i} = \left(\frac{NT}{(1-\lambda)NT + \lambda} \right)^{\frac{1}{2}} \times f_{C_r} \times f_{PR} \tag{18}$$

with $$\lambda = 1 - \left(1 + 16.6\, C_r / L_i\right)^{-2} \tag{6}$$

and f_{Cr} and f_{PR} obtained from a curve fitting process

$$f_{C_r} = \left(0.1528 \times \frac{C_r / R}{0.00272} + 0.8542 \right) \tag{19}$$

$$f_{PR} = \left(0.0833 PR^2 + 0.025 PR + 1.087\right) \tag{20}$$

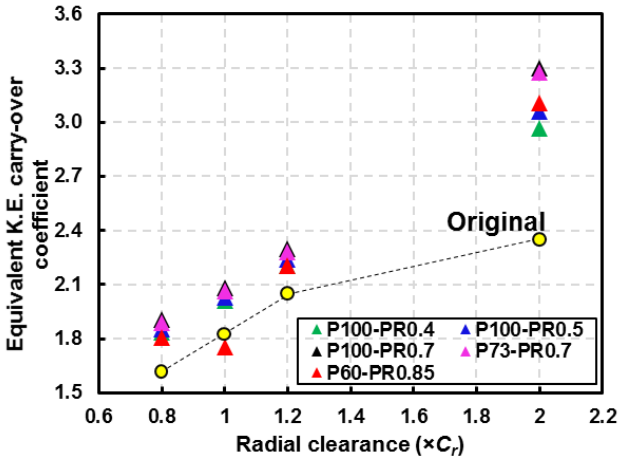

(a) μ_{1i} vs clearance

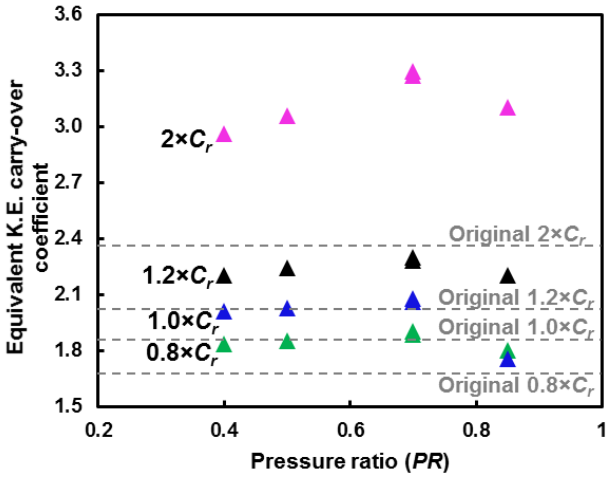

(b) μ_{1i} vs pressure ratio *PR*

Figure 18. CFD derived (averaged) μ_{1i} (a) vs. seal radial clearance; and (b) vs. pressure ratio, *PR*. TOS labyrinth seal with radial clearance = (0.8,1.0,1.2, 2.0)×C_r, supply pressure P_{in} from 60 bar to 100 bar, and pressure ratio *PR* = 0.4 ~ 0.85. Rotor speed Ω = 12 krpm ($R\Omega$ = 138 m/s).

Table 6 lists the mass flow rates predicted by a BFM with the above modified kinetic energy carry-over coefficient model. Figure 19 depicts the CFD and updated BFM predicted mass flow rate and flow factor (ϕ) versus pressure ratio. When compared to the original BFM predictions, the modified model aids to a significant improvement in the mass flow rate predictions, all within 5.4% of the CFD predictions.

Figure 20 shows the updated BFM modified flow factor $\bar{\Phi}$ agrees well with the CFD predictions. Also, the modified model produces an improved accuracy on the prediction of cavity pressures, as shown in Figure 21.

Table 6. Mass flow rate for TOS labyrinth seals: CFD and updated BFM with modified μ_{1i}. Seal radial clearance = (0.8, 1.0, 1.2, 2.0) ×C_r, supply pressure P_{in} = 60 to 100 bar, pressure ratio $PR = P_{out}/P_{in}$ = 0.4 ~ 0.85, and rotor speed Ω = 12 krpm ($R\Omega$ = 138 m/s).

Operating Conditions	Prediction Method	Mass Flow Rate [kg/s]			
		0.8 × Cr	1.0 × Cr	1.2 × Cr	2.0 × Cr
P_{in} =60 bar, PR = 0.85	CFD	0.495	0.606	0.865	1.868
	Modified	0.497	0.609	0.869	1.767
	Diff.	**0.5%**	**0.4%**	**0.5%**	**-5.4%**
P_{in} =72.8 bar, PR = 0.7	CFD	0.835	1.123	1.446	3.081
	Modified	0.839	1.129	1.457	3.083
	Diff.	**0.5%**	**0.5%**	**0.8%**	**0.1%**
P_{in} =100 bar, PR = 0.4	CFD	1.465	1.960	2.525	5.181
	Modified	1.467	1.967	2.532	5.190
	Diff.	**0.1%**	**0.4%**	**0.3%**	**0.2%**
P_{in} =100 bar, PR = 0.5	CFD	1.387	1.859	2.397	4.964
	Modified	1.391	1.868	2.413	4.975
	Diff.	**0.3%**	**0.5%**	**0.7%**	**0.2%**
P_{in} =100 bar, PR = 0.7	CFD	1.153	1.550	2.000	4.246
	Modified	1.163	1.561	2.013	4.252
	Diff.	**0.8%**	**0.7%**	**0.7%**	**0.1%**

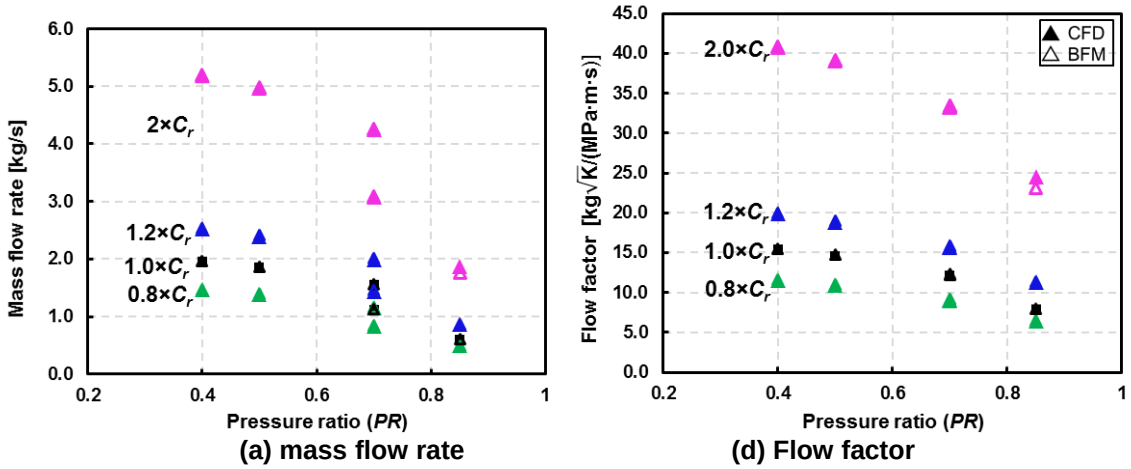

Figure 19. CFD and updated BFM predicted (a) mass flow rate vs. *PR*; (b) flow factor vs. *PR*. TOS labyrinth seal, radial clearance = (0.8, 1.0, 1.2, 2.0) ×C_r, supply pressure increases from 60 to 100 bar, pressure ratio $PR = P_{out}/P_{in}$ = 0.4 ~ 0.85, and rotor speed Ω = 12 krpm ($R\Omega$ = 138 m/s).

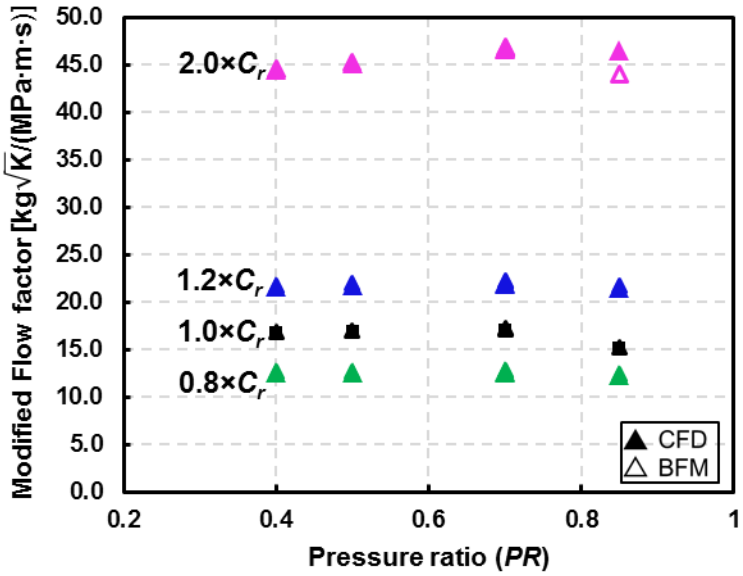

Figure 20. Modified flow factor $\bar{\Phi}$ vs. $PR = P_{out}/P_{in}$ from CFD and updated BFM. TOS labyrinth seal, radial clearance = (0.8, 1.0, 1.2, 2.0) ×C_r, supply pressure increases from 60 to 100 bar, and rotor speed Ω = 12 krpm ($R\Omega$ = 138 m/s).

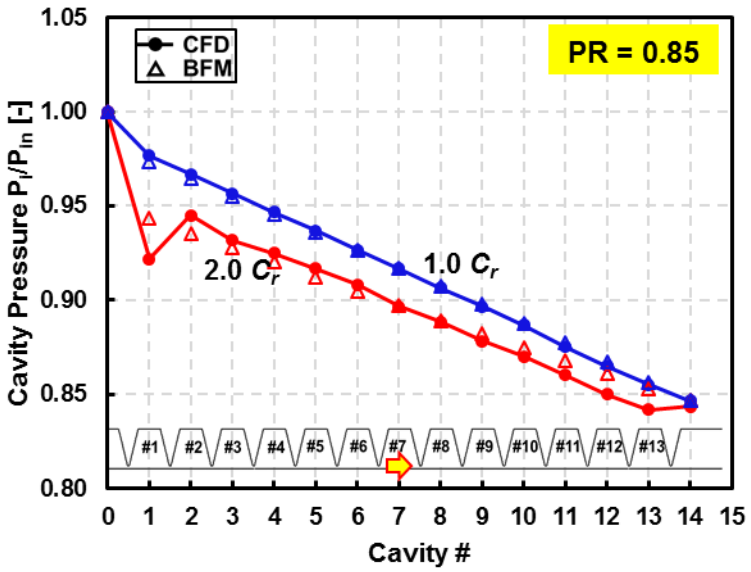

Figure 21. CFD and updated BFM predicted cavity pressure (P_i/P_{in}) vs. cavity #. TOS labyrinth seals with radial clearance = 1.0×C_r and 2.0 ×C_r, rotor speed Ω = 12 krpm, supply pressure P_{in} = 60 bar, pressure ratio PR = 0.85.

7. AN INDEPENDENT CASE FOR VALIDATION

A 14 teeth TOS labyrinth seal tested by Ertas et al. (2012) [36] with a 0.3 mm clearance serves to further validate the updated BFM. In addition, later Li et al. [37] change the clearance of the LS to 0.1 mm and 0.2 mm to predict changes in mass flow rate. The predictions provide more data to validate the modified seal leakage model. Table 7 lists the TOS LS geometry as well as the operating conditions, Ref. [37]. Note the tooth pitch length L_i = 5 mm. Air enters the seal at a supply pressure P_{in} = 6.9 bar (absolute) and room temperature (300 K), and with a pre-swirl velocity $U_0 = 0.5R\Omega$. The seal outlet discharge pressure is P_{out} = 3.0 bar ($PR = P_{out}/P_{in}$ = 0.43).

Figure 22 depicts the mass flow rate versus seal radial clearance C_r. For the smallest clearance C_r = 0.1 mm configuration, the original BFM predicted mass flow rate agrees with the CFD prediction; however, as C_r increases, the discrepancy between the original BFM prediction and the CFD/test results increases from 7% to 14%. The updated BFM with a modified kinetic energy parameter delivers mass flow rates in agreement with the test result (C_r = 0.3 mm) and also with the CFD predicted ones for clearances C_r = 0.1 mm and 0.2 mm.

Table 7. Dimensions and operating conditions of a teeth-on-stator (TOS) labyrinth seal in Ref. [37].

Seal Geometry	Seal length, L	65 mm
	Rotor diameter, D	170 mm
	Radial clearance, C_r	0.1, 0.2, 0.3 mm
	Teeth number, NT	14
	Tooth pitch, L_i	5 mm
	Height, B	4 mm
	Width at tip, b_t	0.3 mm
Air Properties (ideal gas)	Density, ρ @1bar	1.28 kg/m^3
	Temperature, T	300 K
	Sound speed, V_s	314 m/s
	Viscosity, v	1.51×10^{-5} m^2/s
Operating Conditions	Supply pressure, P_{in}	6.9 bar
	Discharge pressure, P_{out}	3.0 bar
	Pressure ratio, $PR= P_{out}/P_{in}$	0.43
	Pre-swirl velocity, U_0	$0.5R\Omega$
	Rotor Speed, Ω ($R\Omega$)	15 krpm (133 m/s)

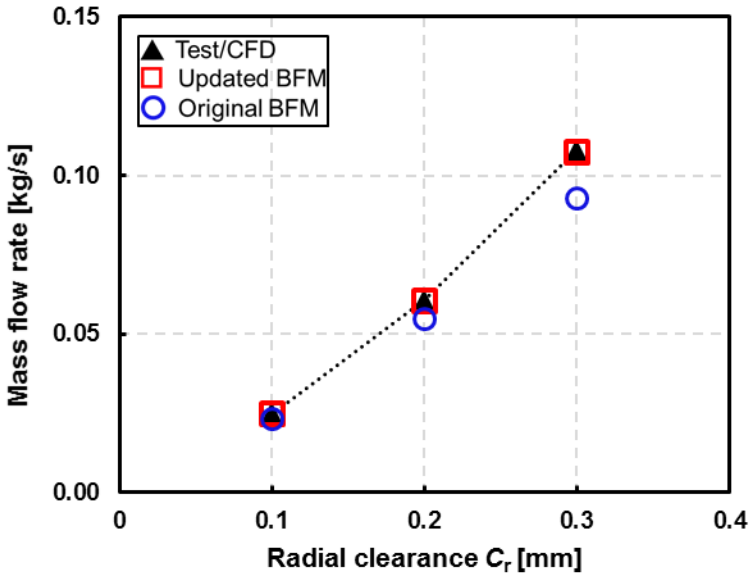

Figure 22. Measured/CFD and BFM (original and updated) predicted mass flow rate vs. radial clearance. TOS labyrinth seal [35,36]: rotor speed Ω = 15 krpm, supply pressure P_{in} = 6.9 bar, pressure ratio PR = 0.43.

8. CLOSURE

This report presents a CFD analysis of a TOS LS to quantify the effect of seal clearance and operating conditions on the kinetic energy carry-over coefficient (μ_{1i}). Based on a TOS LS tested by Vannini et al. [33] in 2014, the seal radial clearance is varied from 0.8 C_r (0.24 mm) to 2 C_r (0.6 mm). In the example, the rotor speed is 12 krpm ($R\Omega$ = 138 m/s), while the supply pressure P_{in} ranges from 60 bar to 100 bar, and the pressure ratio $PR = P_{out}/P_{in}$ varies from 0.40 to 0.85 .

CFD flow predictions show the original bulk-flow model underestimates the actual seal mass flow rate as the kinetic energy carry-over coefficient (μ_{1i}) used is too low. The coefficient (μ_{1i}) is not only a function of the radial clearance (C_r)/cavity length ratio but also depends on the pressure ratio ($PR = P_{out}/P_{in}$), and not the magnitude of either the supply pressure or exit pressure.

A modified kinetic energy carry-over coefficient (μ_{1i}) is derived from the CFD flow predictions via curve-fitting of an averaged μ_{1i}. Integration of the relation into a BFM code improves its accuracy to predict LS mass flow rate as well as cavity pressures. The original kinetic energy carry-over coefficient (μ_{1i}) model under-estimates the mass flow rate by up to 19%, while the current modified model predicts the flow rate within 6% of the CFD predictions. Besides, the modified BFM predicted cavity pressures shows a better agreement with the CFD predictions.

The modified BFM also produces leakage in agreement with measurements for another seal tested by Ertas et al. (2012) [36]. The results for this LS certify the generality of the approach.

9. NOMENCLATURE

a_r, a_s	Dimensionless length defined in Eqn.(3).
A	Cross-sectional area of the cavity [m^2]
b_t	Tooth width [mm]
B	Height of the labyrinth seal strip [mm]
C_r	Radial clearance [mm]
D	Rotor diameter [mm]
L	Seal length [mm]
L_i	Pitch length [mm]
NT	Number of tooth
P_i	i^{th} cavity pressure [Pa]
P_{in}, P_{out}	Supply/discharge pressure [Pa]
PR	Pressure ratio, $PR= P_{in}/P_{out}$
R_g	Gas constant
R	Rotor radius [mm]
T	Temperature [K]
U	Bulk-flow circumferential velocity in a cavity in Eqn.(3) [m/s]

U_{rotor}	Rotor surface velocity $U_{rotor} = R\Omega$ [m/s]
U_0	Inlet pre-swirl velocity [m/s]
α	Inlet pre-swirl ratio, $\alpha = U_0/(R\Omega)$
γ	Specific heats ratio
θ	Circumferential direction
μ_{1i}	Kinetic energy carry-over coefficient
μ_{2i}	Flow discharge coefficient
ν	Kinematic viscosity $\nu = \mu/\rho$ [m^2/s]
ρ	Density [kg/m^3]
ρ_s	Density at supply pressure[kg/m^3]
τ	Shear stress [N]
Ω	Rotor speed [rpm]

Subscripts

i	i^{th} chamber value
r	Rotor surface
s	Stator surface

Abbreviations

BFM	Bulk-flow model
CFD	Computational fluid dynamics
LS	Labyrinth seal
TOS	Tooth on stator labyrinth seal

10. REFERENCES

[1] Ek, M., 1978, "Solution of the Subsynchronous Whirl Problem in the High-Pressure Hydrogen Turbomachinery of the Space Shuttle Main Engine," 14th Joint Propulsion Conference,Las Vegas, July 25-27, pp. 100201-100226.

[2] Childs, D. W., 1993, *Turbomachinery Rotordynamics: Phenomena, Modeling, and Analysis*, Chap.5, "Rotordynamic Models for Annular Gas Seals", John Wiley & Sons, pp. 209-306.

[3] Kuwamura, Y., Matsumoto, K., Uehara, H., Ooyama, H., Tanaka, Y., and Nishimoto, S., 2013, "Development of New High-Performance Labyrinth Seal Using Aerodynamic Approach," ASME Paper GT2013-94106.

[4] Gao, R., and Kirk, G., 2013, "CFD Study on Stepped and Drum Balance Labyrinth Seal," Tribol T, **56**(4), pp. 663-671.

[5] Childs, D. W., Elrod, D. A., and Hale, K., 1988, "Rotordynamic Coefficient and Leakage Test Results for Interlock and Tooth-on-Stator Labyrinth Seals," ASME Paper 88-GT-87.

[6] Paolillo, R., Moore, S., Cloud, D., and Glahn, J. A., 2007, "Impact of Rotational Speed on the Discharge Characteristic of Stepped Labyrinth Seals," Turbo Expo. 2007, ASME Paper GT2007-28248.

[7] Li, Z., Li, J., Yan, X., and Feng, Z., 2011, "Effects of Pressure Ratio and Rotational Speed on Leakage Flow and Cavity Pressure in the Staggered Labyrinth Seal," ASME J Eng Gas Turb Power, **133**(11), pp. 11450301-11450306.

[8] Gamal, A. J., and Vance, J. M., 2008, "Labyrinth Seal Leakage Tests: Tooth Profile, Tooth Thickness, and Eccentricity Effects," ASME J Eng Gas Turb Power, **130**(1), pp. 01251001-01251011.

[9] Hodkinson, B., 1939, "Estimation of the Leakage through a Labyrinth Gland," Proceedings of the Institution of Mechanical Engineers, **141**(1), pp. 283-288.

[10] Zhang, L., Zhu, H., Liu, C., and Tong, F., 2016, "Experimental and Numerical Investigation on Leakage Characteristic of Stepped Labyrinth Seal," ASME Paper GT2016-56743.

[11] Murphy, B., and Vance, J., 1980, "Labyrinth Seal Effects on Rotor Whirl Instability," Proceedings of the 2nd International Conference on Vibrations in Rotating Machinery,Cambridge, England, September 1-4.

[12] Kostynk, A., 1972, "Theoretical Analysis of the Aerodynamic Forces in the Labyrinth Glands of Turbomachines," Therm Eng, **19**(11), pp. 29-33.

[13] Iwatsubo, T., 1980, "Evaluation of Instability Forces of Labyrinth Seals in Turbines or Compressors," Proceedings of a Workshop on Rotordynamic Instability Problems in High-Performance Turbomachinery,Texas A&M University, College Station, TX, pp. 139-167.

[14] Iwatsubo, T., Motooka, N., and Kawai, R., 1982, "Flow Induced Force of Labyrinth Seal," Proceedings of a Workshop on Rotordynamic Instability Problems in High-Performance Turbomachinery,Texas A&M University, College Station, TX, pp. 205-222.

[15] Childs, D. W., and Scharrer, J. K., 1986, "An Iwatsubo-Based Solution for Labyrinth Seals: Comparison to Experimental Results," ASME J Eng Gas Turb Power, **108**(2), pp. 325-331.

[16] Martin, H., 1908, "Labyrinth Packings," Engineering, **85**(10), pp. 35-38.

[17] Egli, A., 1935, "The Leakage of Steam through Labyrinth Seals," Trans. Asme, **57**(3), pp. 115-122.

[18] Neumann, K., 1964, "Zur Frage der Verwendung von Durchblickdichtungen im Dampfturbinenbau," Maschinenbautechnik, **13**(4), pp. 188-195.

[19] Dai, Y., Tyacke, J., and Tucker, P., 2016, "Effect of Labyrinth Seal Configurations on Leakage Performance using LES," 54th AIAA Aerospace Sciences Meeting, San Diego, California, USA.

[20] Rai, A. C., Prabhudharwadkar, D., Murthy, S., Giametta, A., and Johns, D., 2016, "Effect of Air-Curtains on Labyrinth Seal Performance," Turbo Expo. 2016, ASME Paper GT2016-57188.

[21] Migliorini, P. J., Untaroiu, A., Wood, H. G., and Allaire, P. E., 2012, "A Computational Fluid Dynamics/Bulk-Flow Hybrid Method for Determining Rotordynamic Coefficients of Annular Gas Seals," ASME J Tribol, **134**(2), pp. 0222021-0222029.

[22] Migliorini, P. J., Untaroiu, A., Witt, W. C., Morgan, N. R., and Wood, H. G., 2014, "Hybrid Analysis of Gas Annular Seals with Energy Equation," ASME J Tribol, **136**(3), pp. 0317041-0317049.

[23] Childs, D. W., and Wade, J., 2004, "Rotordynamic Coefficient and Leakage Characteristics for Hole-Pattern-Stator Annular Gas Seals-Measurements versus Predictions," ASME J Tribol, **126**(2), pp. 326-333.

[24] San Andrés, L., Wu, T., Maeda, H., and Ono, T., 2018, "A Computational Fluid Dynamics Modified Bulk-Flow Analysis for Circumferentially Shallow Grooved Liquid Seals," ASME J Eng Gas Turb Power, **140**, pp. 0125041- 0125049.

[25] Nordmann, R., Dietzen, F. J., Janson, W., Frei, A., Florjancic, S., 1986, "Rotordynamic Coefficients and Leakage Flow of Parallel Grooved Seals and Smooth Seals."

[26] Cangioli, F., Vannini, G., Pennacchi, P., Ciuchicchi, L., Nettis, L., and Chatterton, S., 2018, "Rotordynamic Characterization of a Staggered Labyrinth Seal: Experimental Test Data and Comparison with Predictions," ASME J Eng Gas Turb Power, **141**(1), pp. 01100901-01100912.

[27] Wu, T., and San Andrés, L., 2019, "Gas Labyrinth Seals: on the Effect of Clearance and Operating Conditions on Wall Friction Factors – a CFD Investigation," Tribol Int, **131**, pp. 363-376.

[28] San Andrés, L., Wu, T., Barajas-Rivera, J., Zhang, J., and Kawashita, R., 2019, "Leakage and Cavity Pressures in an Interlocking Labyrinth Gas Seal: Measurements vs. Predictions," ASME paper GT2019-91507.

[29] Childs, D. W., 1993, *Turbomachinery Rotordynamics: Phenomena, Modeling, and Analysis*, Chap.4, "Rotordynamic Models for Annular Gas Seals", John Wiley & Sons.

[30] Gurevich, M. I., 1966, *The Theory of Jets in an Ideal Fluid*, Pergamon Press, Oxford, pp. 235-256.

[31] Yèucel, U., 1996, "Leakage and Swirl Velocities in Labyrinth Seals," M.S. Thesis, Department of Applied Mathematics, Lehigh University.

[32] San Andrés, L., 1991, "Analysis of Variable Fluid Properties, Turbulent Annular Seals," ASME J Tribol, **113**(4), pp. 694-702.

[33] Vannini, G., Cioncolini, S., Del Vescovo, G., and Rovini, M., 2014, "Labyrinth Seal and Pocket Damper Seal High Pressure Rotordynamic Test Data," ASME J Eng Gas Turb Power, **136**(2), pp. 022501-022509.

[34] San Andrés, L., and Wu, T., 2017, "An Improved Bulk-Flow Analysis for Interlocking Labyrinth Gas Seals: Leakage and Force Coefficients," A Technical Report to Turbomachinery Research Consortium (TRC), June 2017, Report No. TRC-Seal-02-17.

[35] Delgado, I., and Proctor, M., 2006, "Continued Investigation of Leakage and Power Loss Test Results for Competing Turbine Engine Seals," 42nd AIAA/ASME/SAE/ASEE Joint Propulsion Conference & Exhibit, Sacramento, California, July 9-12. Paper number: AIAA–2006–4754.

[36] Ertas, B. H., Delgado, A., and Vannini, G., 2012, "Rotordynamic Force Coefficients for Three Types of Annular Gas Seals with Inlet Preswirl and High Differential Pressure Ratio," ASME J Eng Gas Turb Power, **134**(4), pp. 04250301-04250312.

[37] Li, Z., Li, J., and Feng, Z., 2016, "Labyrinth Seal Rotordynamic Characteristics Part II: Geometrical Parameter Effects," J. Propul. Power, pp. 1281-1291.